International Journal of Hydrogen Energy 59 (2024) 176–186

Contents lists available at ScienceDirect

International Journal of Hydrogen Energy

journal homepage: www.elsevier.com/locate/he

Morphological analysis of iridium oxide anode catalyst layers for proton exchange membrane water electrolysis using high-resolution imaging

Kara J. Ferner [a], Janghoon Park [b], Zhenye Kang [b], Scott A. Mauger [b], Michael Ulsh [b], Guido Bender [b], Shawn Litster [a,*]

[a] Department of Mechanical Engineering, Carnegie Mellon University, 5000 Forbes Avenue, Pittsburgh, PA 15213, USA
[b] Chemistry and Nanoscience Center, National Renewable Energy Laboratory, 15013 Denver West Parkway, Golden, CO 80401, USA

ARTICLE INFO

Keywords:
Proton exchange membrane electrolysis
Anode catalyst layer
Morphological characterization
X-ray computed tomography
pFIB-SEM

ABSTRACT

This work demonstrates the application of high-resolution, 3D imaging to characterize micro- and nano-scale features of iridium oxide (IrO_2) anode catalyst layers (CLs) in proton exchange membrane water electrolysis (PEMWE). Scanning electron microscopy (SEM) and nanoscale X-ray computed tomography (nano-CT) reveal differences in micro-scale features between spray-coated and blade-coated CLs, and in blade-coated CLs along the fabrication and testing timeline. The electrode thickness distribution of the tested blade-coated CL suggests increased thinning of regions compressed by titanium fibers of the porous transport layer (PTL). Ultra-high-resolution imaging of Xe-plasma focused ion beam with SEM (pFIB-SEM) with the development of a segmentation method is used to investigate nano-scale features between these regions of the tested blade-coated CL, showing variations in porosity and pore sizes. The findings provide insights and modeling inputs for the morphology of PEMWE anode CLs towards a better understanding of the relationship between fabrication, operation, and transport behavior.

1. Introduction

Using hydrogen as a clean energy carrier is an extremely promising method for decarbonizing industrial processes, the transportation sector, and the electric grid [1–3]. However, the cost to produce low-carbon hydrogen must be lowered to compete with traditional fossil fuels. One promising technology for low-carbon hydrogen production is proton exchange membrane water electrolysis (PEMWE). PEMWE converts electrical energy into chemical energy by splitting water into hydrogen and oxygen, where the hydrogen can be stored and used later as fuel, such as in a fuel cell vehicle, or it may be used as energy storage for highly intermittent renewables such as wind and solar [2–5]. However, one of the main challenges of PEMWE is the high cost of materials, particularly of iridium used in the anode catalyst layer (CL).

In a PEM electrolyzer, the water is supplied as the reactant to the anode where it is split into oxygen, protons, and electrons via the oxygen evolution reaction (OER). Given the unfavorable kinetics of the OER as well as the corrosive and acidic environment at the anode, the anode catalyst material must be highly active and stable. Iridium in the form of iridium oxide (IrO_2) is one of the few catalysts that meets both these high activity and stability requirements and has become the current state-of-the-art anode catalyst [3,6]. However, with an annual global production of only about 7 tons, iridium is one of the rarest elements on Earth [7,8]. This significantly drives up costs and introduces potential limitations in reaching widespread commercialization of PEMWE systems.

The two primary pathways for improving iridium-specific power density are to directly lower iridium loadings and to improve the utilization of iridium for higher current density operation. Current state-of-the-art PEMWE systems operate with iridium loadings of 1 to 3 mg_{Ir} cm^{-2}, but near-term goals for lower loadings reach below 0.5 mg_{Ir} cm^{-2} [2]. However, achieving high current densities at lower iridium loadings is challenging in practice due to the complex transport phenomena that must occur simultaneously at the anode. Reaction kinetics, the transfer of electrons and protons, and the two-phase flow of liquid water and gaseous oxygen must all be considered when designing and fabricating the PEMWE anode CL [3,4,9]. For PEM electrolyzers as well as other electrochemical devices such as PEM fuel cells, solid oxide fuel cells, and batteries, the microstructure of electrodes largely affects electrochemical performance [10–18]. Thus, understanding and optimizing the morphology and microstructure of IrO_2 CLs will be vital for practical realization of lower iridium loadings and higher current density operation.

Recent studies have focused on evaluating fabrication methods for lower iridium loadings. Taie et al. [8] demonstrated high specific power

* Corresponding author.
E-mail address: litster@andrew.cmu.edu (S. Litster).

https://doi.org/10.1016/j.ijhydene.2024.02.020
Received 31 October 2023; Received in revised form 18 January 2024; Accepted 2 February 2024
Available online 7 February 2024

density with loadings as low as 0.011 mg_{Ir} cm^{-2} by using a suite of characterization techniques to optimize spray coating of their CLs. Alia et al. [19] compared several ink formulation and spray coating parameters through electrochemical characterization, while Khandavalli et al. [20] investigated how the rheology of inks with various catalyst to ionomer concentrations affected resulting catalyst particle microstructure, all showing that CL fabrication choices can have significant impacts on electrolyzer performance through microstructural changes. Other methods for achieving low iridium loadings include dispersing iridium on high surface area supports, such as TiO_2 [21–23], but this often comes at the expense of electrical conductivity and/or stability. Additionally, novel techniques have been investigated such as nanostructured thin films (NSTF) [24], nanofiber interlayers [25], or core–shell catalyst structure [26], but these methods still require significant development.

Thus far, imaging-based morphology studies in the PEMWE space have primarily focused on the titanium porous transport layers (PTLs) used as the anode gas diffusion media [27–31]. Microscale X-ray computed tomography (micro-CT) has been widely used (in combination with modeling and electrochemical characterization) to establish that bulk PTL properties can impact mass transport via oxygen removal and distribution [29,30] and that high interfacial contact between the PTL and CL is crucial for providing sufficient electrical percolation networks to minimize ohmic losses [27,31]. While micro-CT is well suited for imaging titanium PTLs which are around 250 μm thick, IrO_2 CLs are comparatively much thinner on the order of 1 to 10 μm and have particle features as small as tens of nm. Thus, resolving the relevant micro and nanoscale features of IrO_2 CLs requires the use of higher resolution imaging techniques such as nanoscale XCT (nano-CT) and plasma-focused ion beam with scanning electron microscopy (pFIB-SEM).

Nano-CT uses advanced diffraction-based X-ray optics with a lab-scale 8 keV rotating copper anode source, enabling non-destructive, internal 3D imaging [32]. The lab-scale nano-CT can achieve spatial resolutions as high as 50 nm using a Fresnel zone plate objective lens. Epting et al., Braaten et al., and others demonstrated successful use of nano-CT to image PEM fuel cell CLs, typically made of a platinum on carbon catalyst with Nafion ionomer [15,33–36]. The use of Zernike phase contrast imaging has also been reported to image low-Z materials such as platinum group metal (PGM)-free catalysts and to provide high contrast between solid and pore phases [37,38].

pFIB-SEM uses a xenon-plasma ion beam to serially remove small slices of material and is coupled with an electron beam to acquire a stack of 2D SEM images representing a 3D volume. pFIB-SEM has primarily been used for solid oxide fuel cell CLs for imaging large regions up to ~125 × 75 × 15 $μm^3$ [16–18] and has also been used for PGM-free PEM fuel cell CLs, demonstrating ultra-high-resolutions of 2 nm pixels and 4 nm slice thicknesses [39]. To our knowledge, the only reported FIB-SEM imaging of a PEMWE anode CL was demonstrated by Hegge et al. [40], in which gallium FIB-SEM was used to image a 29 × 24 × 7 $μm^3$ volume of IrRuOx catalyst. Compared to gallium FIB-SEM technology, pFIB-SEM can achieve faster material removal rates, larger volume sizes, and avoids sample contamination problems from the heaver gallium ions. Compared to nano-CT, the two main drawbacks of pFIB-SEM are that it is a destructive imaging technique and it requires more challenging sample preparation and post-processing/segmentation [16].

In this study, we used nano-CT and pFIB-SEM to characterize PEMWE IrO_2 CLs for morphological analysis at both the electrode (micro) scale and primary particle/pore (nano) scale. First, we used nano-CT to compare two CL coating methods (spray coating and blade coating) and to compare three steps of blade-coated CLs along the fabrication and testing timeline. Using a spatial resolution of 150 nm for nano-CT imaging, electrode scale morphologies were characterized, and electrode thickness distributions were compared. Comparison of nano-CT 3D reconstructions of blade-coated pristine vs. tested CL samples revealed that the tested CL contained regions with increased thinning caused by being under compressed contact with the PTL titanium fibers during electrolyzer assembly and operation. To investigate differences between these varying regions of thickness within the same tested CL and to compare to a pristine CL fabricated by the same method (blade coating), pFIB-SEM was then used with an ultra-high-resolution of 6 nm voxels, allowing for characterization of primary particle/pore scale features that were unresolved by the 150 nm nano-CT resolution. Given the lack of a robust and universal segmentation method for pFIB-SEM data, we developed and assessed an in-house segmentation method via a region-of-interest (ROI) convergence study and parameter sensitivity analysis. Using our developed segmentation method, we successfully quantified differences in porosity and pore-size distributions (PSDs) between regions of heterogeneity within blade-coated CLs. This work demonstrates progress in using 3D, multiscale, high-resolution imaging techniques to identify relationships between fabrication and morphology of IrO_2 CLs.

2. Experimental section

2.1. Electrode fabrication

Electrodes were fabricated by coating an IrO_2 catalyst layer onto a PTFE substrate and then transferring it to a Nafion 117 membrane. The inks were prepared by dispersing IrO_2 catalyst (Alfa Aesar, 99.99% metal basis, Ir 84.5% min; Thermo Fisher Scientific, Haverhill, MA) in a 1:1 w/w mixture of water and 1-propanol, followed by the addition of Nafion D2020 (1000 EW, Ion Power Inc., New Castle, DE) to achieve an ionomer-to-catalyst (I/C) ratio of 0.2. For blade coating, inks were prepared with 20 wt% IrO_2 and the catalyst was dispersed using a high-shear rotor stator mixer (IKA Turrax T25, 18G mixing element; Wilmington, NC) for 15 min at 10,000 rpm. Following mixing, the catalyst ink was cast onto PTFE substrate using an adjustable film applicator with a coating gap of 40 μm. The blade was translated with a speed of 35 mm s^{-1}. The catalyst layers were dried in an oven at 60 °C for 15 min. For spray-coated samples, inks were prepared with a concentration of 2.75 mg_{IrO_2} mL_{ink}^{-1}, and the catalyst was dispersed by tip sonicating for 30 s followed by bath sonication (with ice) for 1 h. The spray-coated catalyst layers were prepared by spraying the catalyst layer onto PTFE substrate using a Sono-tek spray coating station with a 25 kHz Accumist nozzle. The catalyst ink was coated at a flow rate of 0.2 mL min^{-1} with a translational speed of 50 mm s^{-1}. The PTFE substrate was held in place with a heated vacuum plate set to 80 °C.

To transfer the catalyst layer to the membrane, the catalyst layer decal and membrane were sandwiched between two sheets of 1/16″ thick Gylon (7.5 × 7.5 cm) with polyimide film separating the membrane and decal from the Gylon. The decal was transferred to the membrane using a heated press with a pressure of 25 kg cm^{-2} for 3 min at 125 °C. All anode catalyst layers were fabricated to have an iridium loading of approximately 0.35 to 0.40 mg_{Ir} cm^{-2}, verified using X-ray fluorescence (XRF) measurements. Cathode catalyst layers were sprayed directly onto the membranes as described previously [41].

For tested samples, the catalyst-coated-membranes (CCMs) were assembled in cell hardware adjusted to a torque of 40 in-lb. Titanium fiber PTL that was coated with platinum by the manufacturer (Bekaert, 2GDL10-0.25) was used for the anode and a carbon fiber GDL (Toray, MGL280) was used for the cathode. The cells were broken in and conditioned through current density holds followed by a series of polarization curves.

2.2. Nanoscale X-ray computed tomography

The lab-scale nano-CT (UltraXRM L200, Xradia, Inc., Pleasanton, CA) at CMU uses an 8 keV X-ray source to produce low-energy X-rays, allowing for non-destructive imaging. The nano-CT has two modes of contrast imaging: (1) absorption contrast mode and (2) Zernike phase

contrast mode. The contrast of radiographs in absorption contrast mode is determined by the differences in attenuation of X-rays through the sample material, governed by the material's atomic number (Z) and the thickness of material. This allows for good contrast when imaging high-Z materials, such as PGMs (iridium Z = 77, platinum Z = 78). For imaging low-Z materials, Zernike phase contrast uses a Zernike phase ring placed after the objective lens which produces a $3\pi/2$ phase shift of undiffracted X-rays to increase contrast at material or phase interfaces [32]. The nano-CT also provides two resolutions. Large-field-of-view (LFOV) mode has a field of view of 65 μm and spatial resolution of 150 nm, and high-resolution (HRES) mode has a field of view of 16 μm and spatial resolution of 50 nm.

Each sample was prepared by using microscopy grade razor blades to cut a small triangular area of approximately 2 mm in base and 1.5 mm in height (in-plane orientations of the CL), then using epoxy to glue the triangle to the tip of pin fit for the nano-CT sample holder. For this work, LFOV mode was used. With the sample in the nano-CT, the orientation of the CLs is easily identifiable for two reasons. The first is that the through-plane thickness of the CLs is on the order of 1–5 μm, while the in-plane thickness is orders of magnitude larger, defined by the sample preparation cuts. The second reason is that with the use of LFOV, the entire through-plane thickness is contained fully within the 65 μm FOV between regions of air and Nafion membrane which both have a much lower attenuation coefficient compared to the high-Z iridium in the CL, so the thin film orientation of the CL is apparent.

Each tomographic scan was taken with 451 radiograph images from −90° to 90° of sample rotation, with an exposure time of 270 s per image. Because the samples were on Nafion membrane, which can deform during X-ray imaging causing electrode sample movement that results in poor quality reconstructions, the nano-CT scans were done at a location slightly below the triangle tip, which helped improve sample stability during imaging. Lastly, this work used Zernike phase contrast mode. Although iridium is a high-Z material, in preliminary imaging, Zernike phase contrast provided better contrast between solid and pore/void regions and provided greater stability for higher quality reconstructions.

2.3. Plasma-focused ion beam with scanning electron microscopy

The DualBeam Helios pFIB-SEM (FEI Company, Hillsboro, OR) and the commercial 3D acquisition package "AutoSlice and View" (FEI Company, Hillsboro, OR) were used in this work. A schematic of the pFIB-SEM volume acquisition can be found in supplementary data. For each sample imaged, a small area of approximately 5×5 mm^2 was cut using microscopy grade razors blades and mounted to an SEM sample stub, then sputtered with 2 nm of gold to ensure conductivity. One placed within the pFIB-SEM, the sample was set to a 4 mm working distance and tilted 52° for imaging. Before imaging, a layer of platinum approximately 2 μm thick was deposited onto the sample surface ROI to protect the CL during ion beam milling and to mitigate curtaining effects. For sample milling, the ion beam was operated at an accelerating voltage of 30 keV and current of 1.8 nA. For SEM images, the through-lens detector (TLD) was used at an accelerating voltage of 10 keV and operating current of 0.34 nA. A voxel size of $6 \times 6 \times 6$ nm^3 was used and resulting volumes of approximately $10 \times 3 \times 2$ μm^3 were acquired for each sample and reconstructed using in-house image-processing and segmentation described below in the following section. Internal volumes were then down selected for consistency and to save computational time for post-processing and analysis.

2.4. Image-processing and segmentation

Nano-CT images were reconstructed using proprietary software (Xradia, Inc., Pleasanton, CA) and reconstructed volumes were processed for 3D visualization and segmented using Avizo (Thermo Fisher Scientific, Waltham, MA). Given their resolution of 150 nm, Nano-CT reconstructions were used only for electrode thickness measurements, not for primary particle/pore analysis. Thus, the goals of the post-processing steps for the nano-CT reconstructions were to fill in the pore spaces as solids and segment out the entire CL from the surrounding air and Nafion membrane. The image-processing grayscale operations used were a Gaussian smoothing filter followed by a closing morphological operation to fill in the pore space, then a grayscale thresholding to segment the CL. This method allows for electrode thickness measurements to be unaffected by existing pore space while keeping the integrity of the CL-air and CL-membrane interfaces and changes in thickness throughout the imaged region.

pFIB-SEM data is comparatively much more difficult to reconstruct into a segmented 3D volume. While the nano-CT reconstruction is processed directly on the 3D data file, pFIB-SEM data must be reconstructed slice-by-slice for every 2D SEM image in the 3D volume. Additionally, challenges arise during segmentation due to the nature of SEM images; that is, SEM images inherently capture some solid features within the pore space of the material below the foremost 2D plane. Therefore, it is difficult to capture only the desired solid features at each thin 2D slice created by the pFIB milling. Thus, segmentation of pFIB-SEM data must take this into careful consideration and minimize inaccurate segmentation caused by these effects. We developed an in-house image-processing and segmentation method for pFIB-SEM data to effectively remove these types of artifacts, using both MATLAB (Mathworks, Natick, MA) and open-source ImageJ software, and it is briefly described herein.

Each stack of 2D SEM images was first cropped and aligned using image registration, and the grayscale histogram of each image was normalized to the histogram of a selected reference image for consistent contrast and brightness. Due to the pFIB-SEM instrument's 52° incidence angle between the electron beam and the sample cross-section plane of imaging, the effect of imaging the visible solid features below the plane of interest were realized in the resulting 3D volume as 52° streaks artifacts. To remove these artifacts, the image stack was rotated by 52° then "resliced" using ImageJ, such that each 2D image was then parallel to the streak artifacts allowing segmentation to effectively remove them.

After these initial image-processing steps, the segmentation method then binarized the 3D volume into solid and pore phases. The following description outlines the six main steps of our in-house segmentation method using MATLAB. The first four steps were processed on each of the 52° "resliced" 2D images individually and the final two steps were processed on the full 3D volume. First, a Gaussian smoothing filter was used to reduce noise. Second, a forward gradient threshold in the direction of the streak artifacts was used. For each image, the forward gradient method determines the intensity of the change in grayscale values between neighboring pixels. Then, thresholding to select only the sharp transitions from dark to light grayscale values (higher gradient values) effectively selects where the solid CL regions were imaged at the foremost 2D plane and ignores the streak artifacts with more gradual grayscale value transitions (lower gradient values). Third, a low-grayscale-value-removal labeled all pixels with grayscale values below a certain low threshold as pore; and fourth, a high-grayscale-value-addition labeled all pixels above a certain high threshold as solid. This was done to mitigate any nonphysical representations occurring at the grayscale extremes from the gradient threshold step. The fifth step cleaned the stack by using a 3D spherical element for opening and closing operations, and the sixth step was a final 3D Gaussian smoothing filter. A schematic of this process can be found in the supplementary data.

2.5. Morphological analysis

Morphological properties of electrode thickness distributions, PSDs, and porosity were calculated using Porespy, an open-source Python package [42]. For electrode thickness distributions, the Porespy local

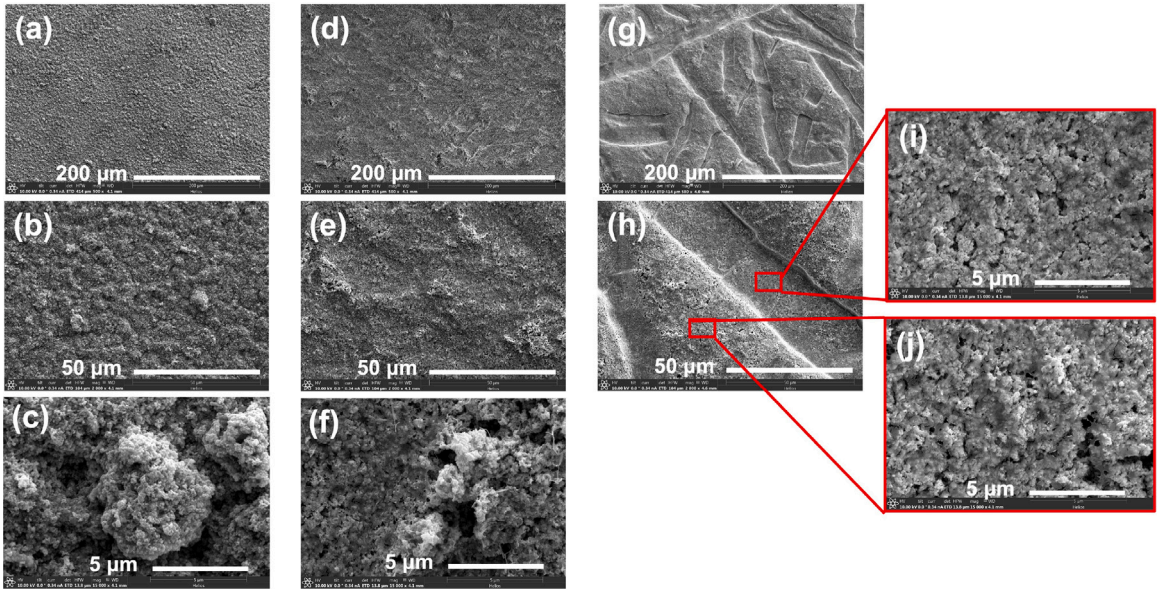

Fig. 1. 2D surface SEM images of (a–c) pristine spray-coated CL, (d–f) pristine blade-coated CL, and (g-j) tested blade-coated CL. The tested blade-coated CL contains (i) PTL-fiber-compressed and (j) PTL-pore-area regions.

thickness filter was processed through the segmented nano-CT volumes, which determines at each voxel the maximum size of an inscribed sphere that fits within the segmented phase, where the diameters of the inscribed spheres corresponded to the electrode thickness values. The same process was used on the pore phase of the segmented pFIB-SEM volumes to calculate PSDs, where in this case the diameters of the inscribed spheres corresponded to the pore diameter values. Using the PSDs, values for mean pore diameter and standard deviation of the pore diameter distribution were calculated. Porosity (ϵ_{pore}) was also determined from the segmented pFIB-SEM volumes, calculated as the number of voxels representing pore space divided by the total number of voxels: ϵ_{pore} = (# of pore voxels)/(# of total voxels).

3. Results and discussion

3.1. Surface SEM images

2D SEM images were first acquired to visualize varying surface topologies between IrO_2 CL samples, shown in Fig. 1. The three CL samples analyzed in this work were: pristine spray-coated, pristine blade-coated, and tested blade-coated CLs. Fig. 1(a–c) shows the pristine spray-coated sample appeared to contain highly spherical catalyst particles and large agglomerates. The blade-coated sample shown in Fig. 1(d–f) on the other hand did not appear to have the same spherical structures, but did contain other rough surface features and heterogeneity. The most noticeable difference in surface features appeared in the tested blade-coated sample in Fig. 1(g–j), showing large indentations tens of μm in width. These indentations in the tested anode CL were a result of contact with the anode titanium fiber PTL under typical electrolyzer cell compression. Compression of the PTL titanium fiber structure into the anode CL effectively partitioned the CL into two distinct regions: regions that were locally compressed due to direct contact with a PTL fiber and regions that were locally uncompressed under the PTL's pore openings. These two locally heterogeneous regions will herein be referred to as "PTL-fiber-compressed" and "PTL-pore-area" regions, respectively. A schematic showing this effect is presented in Fig. 2. Similar effects of anode CL compression from titanium PTLs have been noted by others [43].

It has been established that one of the most important considerations for fabricating CLs is homogeneity, as local heterogeneities and non-uniform CLs can inhibit reactions, cause build ups of evolved oxygen, and result in discontinuous electrical percolation networks [8,43]. The spray coating method has been the primary CL deposition technique for most of the previous research focused on lowering iridium loadings [8,19,44]. The dilute inks needed for spray coating can require multiple spray passes to achieve acceptable thickness and homogeneity of the CL. For this reason, spray coating is suitable for lab-scale research, but is less practical for manufacturing scale-up. Techniques such as blade coating or slot die coating use more concentrated inks and require typically just one pass, making them more suitable for larger-scale production of commercial CLs. Previous work by Park et al. describes the development of a roll-to-roll (R2R) process for direct coating of CLs onto Nafion membrane, a significant advancement for scaling up the production of CCMs and removing the need for a decal-transfer step that often limits blade coating methods [45]. However, efforts to improve homogeneity and optimize blade-coated CLs are still needed.

3.2. Nano-CT imaging

One of the key benefits of nano-CT is the ability for internal 3D imaging of samples [32], as opposed to SEM images which are limited to visualizing 2D surface topology or cross-sections. We first used nano-CT to elucidate possible morphological differences between CL fabrication methods of spray coating versus blade coating. Fig. 3 shows in-plane cross-section images from the nano-CT Zernike phase contrast reconstructions of the (a) pristine spray-coated and (c) pristine blade-coated CLs. Fig. 3(a) shows the spherical agglomerate structure was consistent throughout the spray-coated CL. On the other hand, the nano-CT reconstruction of the pristine blade-coated CL in Fig. 3(c) revealed small primary particle and pore features. Furthermore, both the spray-coated and blade-coated samples contained a few small, bright, highly attenuated regions. These regions indicated either a small particle of high-Z iridium metal appearing brighter in contrast to the IrO_2 particles, or a very dense particle with a high partial volume fraction relative to the rest of the CL. Based on the pFIB-SEM results discussed later, we hypothesize that these high-Z regions indicated the latter; however, additional elemental mapping techniques could be used to investigate the existence of Ir metal content in these CLs.

Nano-CT was also used to investigate any morphological differences along the fabrication and testing timeline of the CL. Three blade-coated samples were imaged that corresponded to three consecutive steps in

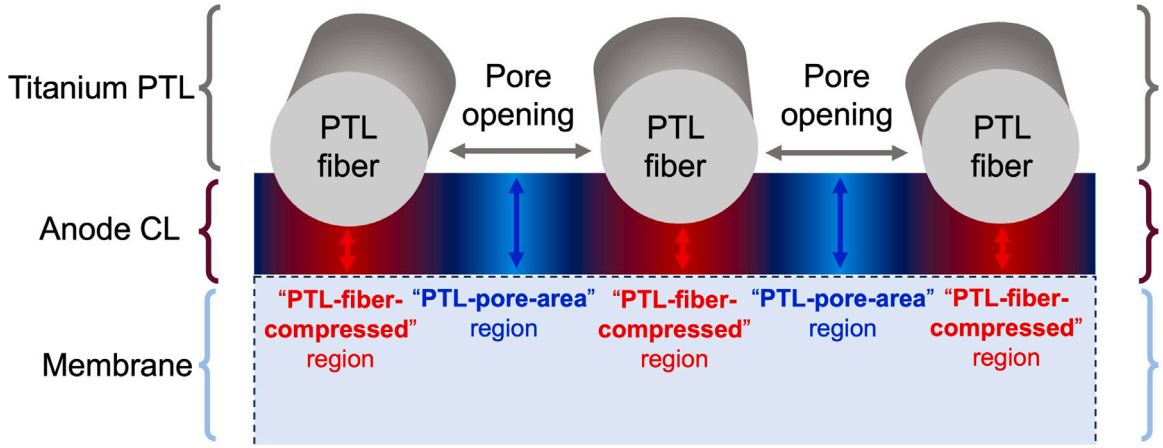

Fig. 2. Schematic depicting the cross-section of the anode of a PEM electrolyzer, where a titanium fiber PTL is used as the anode gas diffusion media. During electrolyzer assembly and operation, the compression applied to the cell causes the PTL fibers to make impressions into the anode CL. We identify two distinct regions in the CL: locally uncompressed regions which were directly under the PTL pore openings (PTL-pore-area regions) and locally compressed regions which were directly under the PTL fibers (PTL-fiber-compressed regions).

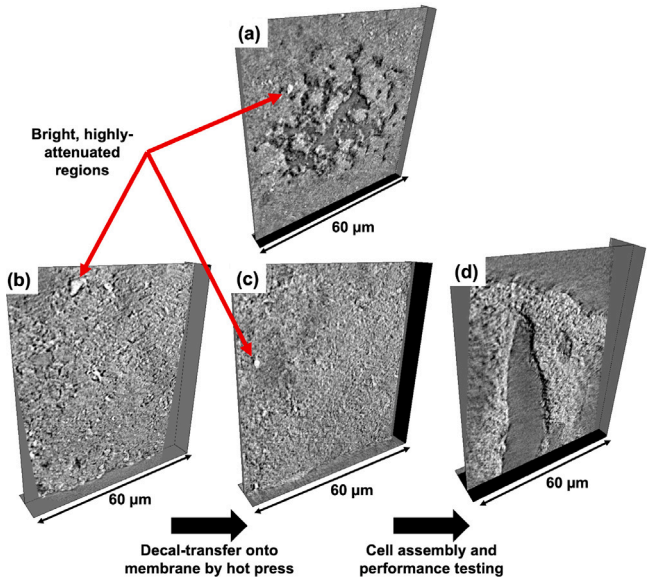

Fig. 3. In-plane cross-sections of nano-CT phase contrast reconstructions. Comparison of fabrication methods shown vertically, with (a) pristine spray-coated CL and (c) pristine blade-coated CL. Comparison of steps along the fabrication and testing timeline of blade-coated CLs shown horizontally, with (b) CL coated onto decal substrate, (c) CL after decal-transfer to membrane via hot-press, and (d) tested CL.

fabrication and testing, shown in Fig. 3: (b) CL coated onto a PTFE decal substrate, (c) CL that was decal-transferred to the membrane by hot pressing (this is also the sample used for comparison to spray coating), and (d) tested CL. First, Fig. 3(b) to (c) shows the CL samples corresponding to immediately before and after the decal-transfer step. Given the visual similarity in electrode thickness, thickness uniformity, and particle size between these nano-CT reconstructions, we concluded that the decal-transfer process did not result in significant morphological changes. No further investigation into this fabrication step was deemed appropriate for this work. However, comparing the pristine blade-coated sample to the tested blade-coated sample using nano-CT validated the existence of significant CL indentations from the titanium PTL fibers.

Videos of the full nano-CT reconstructions associated with each cross-section image shown in Fig. 3 can be found in the supplementary data.

3.3. Electrode thickness

Given the 3D imaging capabilities and field of view that captures the full thickness and electrode scale features of these IrO_2 CLs, nano-CT reconstructions are well suited for analyzing electrode thickness distributions. Electrode thickness analysis was done for the pristine spray-coated, pristine blade-coated, and tested blade-coated CLs. Images of the 3D reconstructions with associated 2D cross sections for each sample are shown in Fig. 4(a-f), with red indicating the thinnest regions of the CLs. Videos of these nano-CT 3D electrode thickness reconstructions can be found in the supplementary data. Fig. 4(g) shows the electrode thickness distribution plot. From the distributions, mean thickness values for each CL were calculated to be 3.39 µm for pristine spray-coated, 4.19 µm for pristine blade-coated, and 2.62 µm for tested blade-coated. The narrower peak of the pristine spray-coated CL thickness distribution compared to that of the pristine blade-coated CL suggests a more uniform thickness, likely a result of the spray passes of thin coatings. Furthermore, the tested blade-coated CL had the smallest mean and maximum thickness value due to the compression of the CL during electrolyzer operation. In addition to the shift of the thickness distribution showing overall thinning for the tested blade-coated layer, the widening of the peak suggests thickness variations between PTL-fiber-compressed and PTL-pore-area regions caused by the PTL titanium fibers and pore openings. In its cross-section image in Fig. 4(f), significant thinning of the CL is seen in regions under the PTL fibers. This highlighted the need to investigate morphological differences that may exist at the primary particle/pore scale between the PTL-fiber-compressed and PTL-pore-area regions of the tested blade-coated CL. However, the nano-CT reconstructions with a spatial resolution of 150 nm are not suited for pore analysis because any pores smaller than 150 nm in diameter would not be resolved. Therefore, nano-CT reconstructions were used solely for analysis of electrode-scale features, while the higher resolution imaging method of pFIB-SEM was needed to conduct appropriate pore scale analysis.

3.4. pFIB-SEM imaging

Previous pFIB-SEM work on solid oxide fuel cell electrodes noted that heterogeneities can exist at different length scales, differentiating between the microscale (tens of µms) and the mesoscale (hundreds of µms) [16,17]. Similarly in PEM electrolyzer anode CLs, heterogeneities can exist both at the electrode (micro) scale and at the particle/pore (nano) scale, and it is important to understand both. While the nano-CT provided electrode scale information, an ultra-high-resolution of

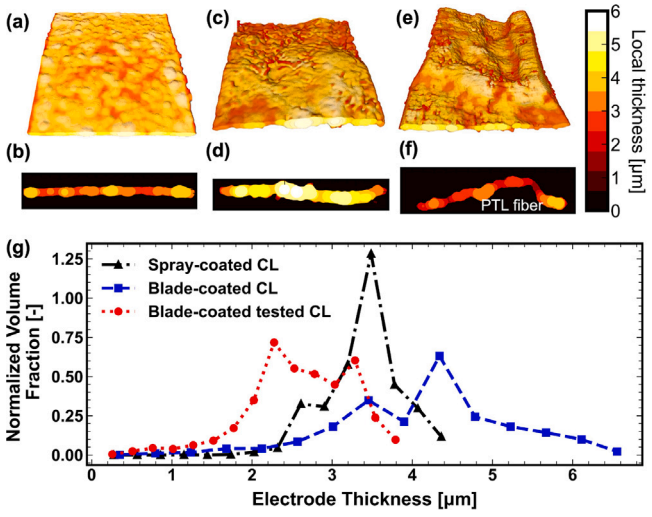

Fig. 4. 3D visualizations and 2D through-plane cross-sections showing local thickness distribution for (a,b) pristine spray-coated CL, (c,d) pristine blade-coated CL, and (e,f) tested blade-coated CL. (g) Electrode thickness distributions for the three analyzed CLs extracted using the nano-CT reconstructions. (For interpretation of the references to color in this figure legend, the reader is referred to the web version of this article.)

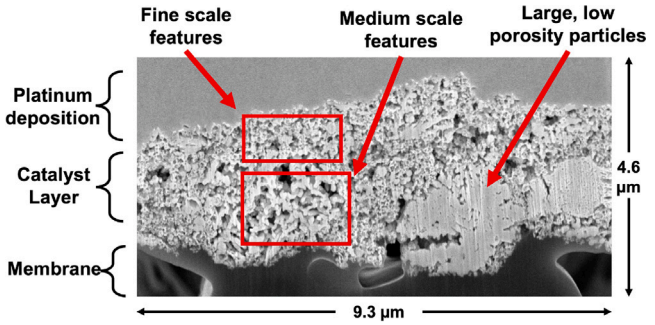

Fig. 5. Example SEM image acquired during pFIB-SEM acquisition of pristine spray-coated CL. The porous structure is the CL, the darker structure below is the membrane, and the smooth structure above is a layer of platinum deposited for sample protection and to mitigate artifacts caused by the plasma ion beam milling. The IrO_2 CLs show a wide range of length scales of particle and pore features, including some very large, low-porosity solid particles that were found across all samples.

6 nm was achieved using pFIB-SEM to study primary particle and pore features. Fig. 5 shows one 2D cross section image of the pristine spray-coated CL, for example. Qualitatively, the pFIB-SEM imaging revealed that these IrO_2 CLs were highly porous and contained varying length scales of primary particle and pore features.

For quantitative analysis at these higher resolutions with pFIB-SEM, we focused only on the blade-coated samples, comparing three distinct regions: (1) a region from the pristine blade-coated sample, and from the tested blade-coated sample, (2) a PTL-pore-area region (under PTL pore openings) and (3) a PTL-fiber-compressed region (under PTL fibers). Fig. 6 shows the pFIB-SEM results for these three regions. Raw 2D SEM cross-section images are shown in Fig. 6(a–c), and full videos showing the slice-by-slice cross-section images can be found in the supplementary data. Fig. 6(d–f) shows the full volume reconstructions produced using the segmentation method described in the Experimental section. Fig. 6(g–i) shows the internal volumes down selected for the data analysis.

All samples, regardless of coating method or fabrication/testing status, appeared to contain large, dense, low-porosity particles like the one shown in Fig. 5, possibly explaining the bright, highly attenuated regions seen in the nano-CT scans (Fig. 3). Furthermore, in agreement with the increased thinning effect seen in the nano-CT electrode thickness analysis, the PTL-fiber-compressed region in Fig. 6(c) appeared to be thinner than the PTL-pore-area region in Fig. 6(b). This is a qualitative insight, because although quantitative analysis of the CL thickness using the pFIB-SEM reconstructions is possible, it would not be appropriate because the volumes acquired through pFIB-SEM were much smaller compared to that of nano-CT. The pFIB-SEM images also suggested that the PTL-fiber-compressed region contained smaller pores than the PTL-pore-area region, warranting the use of segmentation for quantitative pore morphology analysis.

3.5. pFIB-SEM segmentation method assessments

The pFIB-SEM segmentation method developed and used for this work was assessed using a region-of-interest (ROI) convergence study and a parameter sensitivity analysis. The ROI convergence study was used to determine if the selected internal volumes were large enough to provide stable, converging morphological results. Each of the three internal volumes (Fig. 6(g–i)) were increased in size along the longest in-plane direction (10 µm) from 0 to 10 µm by increments of 60 nm (10 voxels). At each increment, values of porosity, mean pore diameter, and standard deviation of pore diameter were calculated and plotted versus the in-plane width. The results of the ROI convergence study in Fig. 7(a) showed that for each of the three regions, all morphological properties converged well before the 10 µm width, suggesting that the selected internal volumes used for this study were sufficiently large in the in-plane width direction to extract reliable data. Similar ROI studies were not done for the other directions of in-plane depth and through-plane due to limitations of the SEM image stack size and the catalyst layer thickness, respectively.

The second assessment of the segmentation method was a sensitivity analysis to determine how each of the input parameters affected the final segmentation and consequently the results of the morphological properties. Most image segmentation methods require some element of user selection; therefore, it is important to assess how the user selections can impact the results. This sensitivity analysis allows for the user to see how different image processing and segmentation parameters may influence the results. There were six important input parameters correlating to each step of the pFIB-SEM segmentation method discussed in the Experimental section. After user selection of the optimal input parameter values, upper and lower bounds for each of the six parameters were determined as the maximum and minimum values which still produced a physical segmentation. For each of the three sample regions and each of the three morphological properties, a sensitivity analysis was plotted to show how changing each segmentation parameter to its upper or lower bound changed the results. This produced nine total plots, which can be found in the supplementary data. Fig. 7(b) shows one of the nine sensitivity analysis plots, for example, of porosity for the pristine CL region. In Fig. 7(b), we find that for our segmentation method, the selection of the gradient threshold value has the greatest impact on porosity for the pristine region, while changing the 3D Gaussian filter value has minimal impact. This sensitivity analysis also allows for significant error analysis of results between the CL regions. It was used to provide error bars for the Fig. 8(a) and (b), where the error bars correspond to the root mean square error of the differences between the input parameters' extreme bounds and the optimal value, as shown in Fig. 7(b) and the supplementary data.

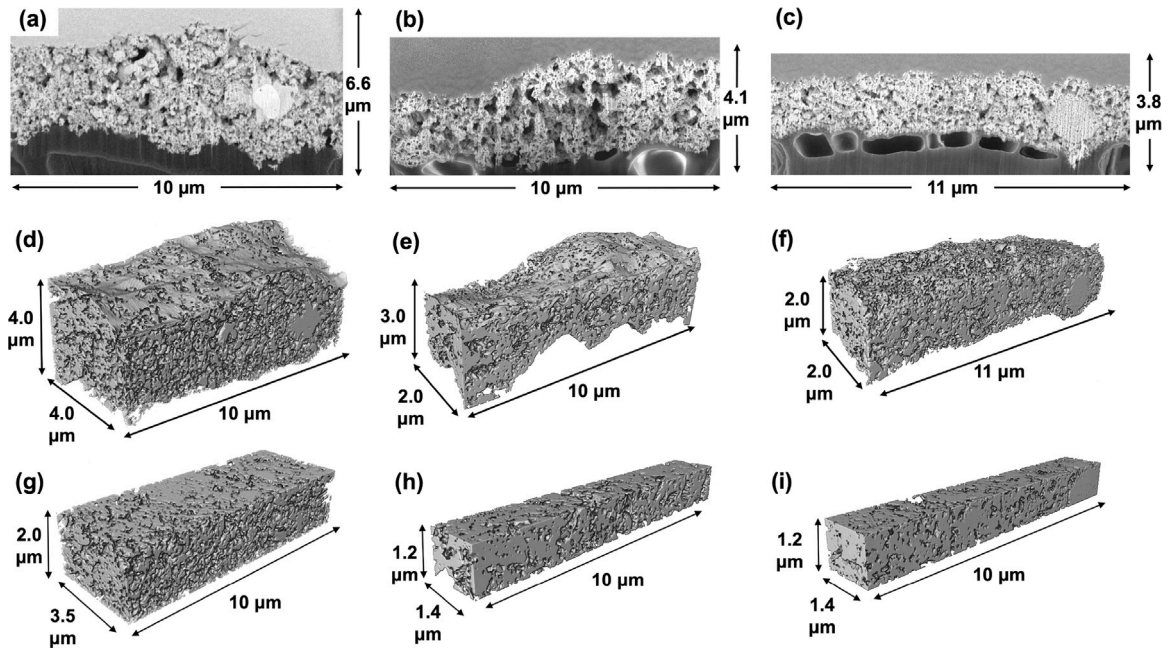

Fig. 6. pFIB-SEM data for (left) pristine blade-coated, (center) PTL-pore-area region of tested blade-coated, and (right) PTL-fiber-compressed region of tested blade-coated CL. (a–c) Raw 2D SEM cross-section images of the CL region, (d–f) full segmented volumes, and (g–i) internal volumes selected for data analysis.

3.6. Pore morphology analysis

For each sample volume in Fig. 6(g–i), porosity and PSDs were determined. From the PSD, the mean and standard deviation of the distributions were also calculated. Fig. 8(a) shows the porosity comparison, Fig. 8(b) shows the mean and standard deviation of pore size comparison, and Fig. 8(c) shows the three PSDs. One of the benefits of PSDs derived from segmented pFIB-SEM data is that unlike with X-ray CT data, the use of direct 2D SEM images allows for the segmentation to be directly compared to each image or "slice" in the stack.

Most notably, the PTL-fiber-compressed region had significantly lower porosity, mean pore diameter, and standard deviation of pore diameter distribution (41.7%, 104 nm, 55.8 nm, respectively) compared to the PTL-pore-area region (55.8%, 166 nm, 114 nm, respectively). This result agrees with the nano-CT electrode thickness analysis which suggested that the PTL-fiber-compressed regions experienced increased thinning, leading to changes in morphological structure. The smaller pore sizes and lower porosity of the PTL-fiber-compressed region could suggest higher in-plane electrical conductivity via improved connectivity of the solid phase, while consequently leading to inhibited mass transport due to fewer pathways for evolved oxygen gas to be removed. Possible differences in ionic conductivity cannot be suggested here as we did not distinguish between phases of the proton-conducting ionomer versus catalyst within the solid phase, but this is an area for future work in morphological analysis.

The calculated porosities of the pristine and PTL-pore-area region were 51.5% and 55.8%, respectively. The maximum pore diameter for both the pristine and the PTL-pore-area region was about 600 nm, shown in the PSD in Fig. 8(c). However, their PSDs also show that the pristine region had higher normalized volume fractions of smaller pore sizes (<150 nm) compared to the PTL-pore-area region. This led to a smaller mean pore diameter for the pristine region of 123 nm, compared to 166 nm for the PTL-pore-area region. Given that the PTL-pore-area region, as part of the tested CL, was under some compression during electrolyzer assembly and operation, it was expected that its porosity and pore size diameter would be equal to or less than that of the pristine region which experienced no compression. However, this was not the case. This result suggests a pathway to investigate the possibility of morphological effects specifically associated with electrochemical outcomes and transport behaviors, which is the subject of ongoing and future work. Image-based modeling can be used to further explore how these differences in pore structure and morphology between the CL regions can impact transport properties and ultimately performance.

Lastly, to further quantify the PSDs presented in Fig. 8(c), each data set was fit to a log normal distribution function, described by:

$$f(x) = \frac{1}{x\sigma\sqrt{2\pi}} \exp\left(-\frac{1}{2}\left(\frac{\ln(x)-\mu}{\sigma}\right)^2\right) \quad (1)$$

where μ is the log normal mean and σ is the log normal standard deviation. The log normal distribution function has been widely used for fitting PSDs for many types of porous media [46–53], and given the skewness of the PSDs shown in this work, the log normal distribution was selected as an appropriate fitting equation. Additionally, we validated the success of the fit with coefficient of determination, R^2, values greater than 0.9 for all CL regions. The log normal mean and standard deviation for each distinct CL region along with their associated R^2 values are reported in Table 1. These PSD fit parameters can be useful for improving the model of the anode CL in future modeling studies of transport properties and performance effects. The use of modeling and simulation has been vital for studying transport phenomena in a variety of electrochemical devices and their components; however, many PEMWE modeling studies assume the anode CL is a thin boundary layer or assume homogeneous pore structure [54,55]. While these have been useful assumptions, it presents limitations to fully elucidating transport properties of practical, heterogeneous CLs with complex morphologies. While image-based and informed stochastic methods for generating more realistic porous components have been demonstrated for modeling PEM fuel cell cathode CLs and PEMWE PTLs [56–61], similar methods for PEMWE IrO_2 CLs models have not yet been widely

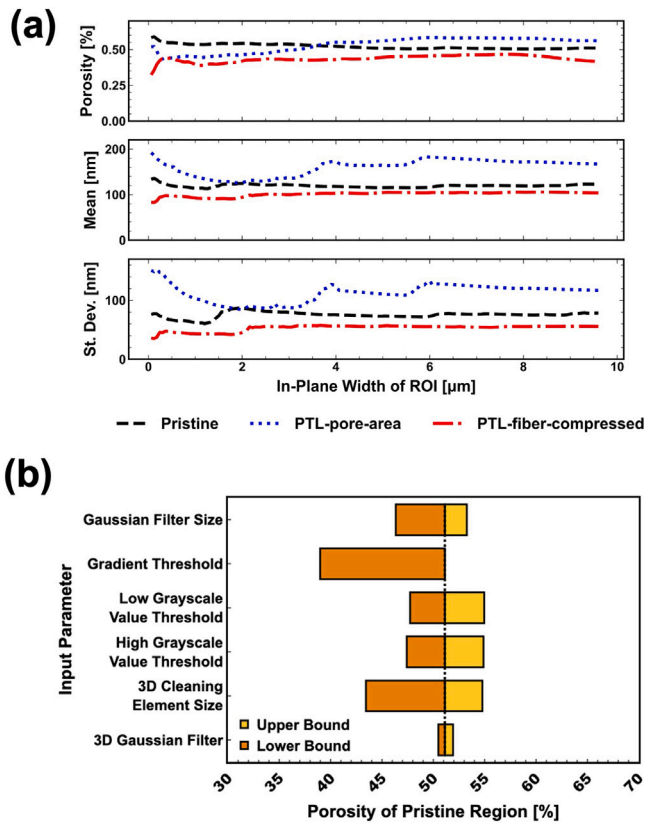

Fig. 7. (a) ROI convergence assessment results. Plots of each pore morphology result (porosity, mean and standard deviation of pore diameter) vs. in-plane width of ROI for all three sample regions. All values converge by approximately 6 μm of in-plane width. (b) Sensitivity analysis plot visualizing the impacts of varying each segmentation method input parameter on the outcome of a particular morphological result. In this case, the plot shows the impacts on the result of porosity for the pristine region. The vertical center line indicates the result calculated when using the optimal values for all input parameters, and the distance of each horizontal bar away from the center line represents the difference in the result between using the extreme bound of that given input parameter and using the chosen optimal value, where the lower bounds are shown in orange and the upper bounds shown in yellow. (For interpretation of the references to color in this figure legend, the reader is referred to the web version of this article.)

Table 1
Parameters and R^2 values for the log normal fit to PSDs.

	μ	σ	R^2
Pristine	4.657	0.6352	0.9844
PTL-pore-area	4.926	0.7396	0.9566
PTL-fiber-compressed	4.572	0.6127	0.9404

adopted. The log normal mean, μ, and standard deviation, σ, presented here for the three distinct CL regions can be used for generating the specific PSDs for more realistic pore network models. Additionally, PSDs can also be quantified experimentally through methods such as mercury porosimetry which is an area of possible future work on precise porosimetry results on thin electrodes.

4. Conclusions

Developing PEMWE anode CLs that can achieve high current density operation at low iridium loadings will require a better understanding of the CL morphology and its relationship with fabrication and performance. In this work, we used two methods of high-resolution, 3D imaging to characterize IrO_2 CLs for morphological analysis. Nano-CT was used to investigate electrode (micro) scale differences between spray-coated and blade-coated CLs as well as between blade-coated CLs at different steps in the fabrication and testing timeline. Electrode thickness distributions were calculated from nano-CT reconstructions, where the pristine spray-coated sample showed a more uniform thickness compared to the pristine blade-coated sample. Additionally, the tested blade-coated sample was the thinnest sample of the three and showed possible differences in thickness values between PTL-pore-area and PTL-fiber-compressed regions caused by contact with the titanium fibers of the PTL. Higher resolution imaging was then achieved with pFIB-SEM and used to further investigate morphological differences at the primary particle/pore (nano) scale. A region of the pristine blade-coated sample was compared to PTL-pore-area and PTL-fiber-compressed regions of the tested blade-coated sample. The PTL-fiber-compressed region had significantly lower porosity, mean and standard deviation of pore diameter compared to the PTL-pore-area region. It was also found that the pristine sample and the PTL-pore-area region had similar porosities and maximum pore diameters (approximately 600 nm), while the PTL-fiber-compressed region had significantly lower porosity and maximum pore diameter (300 nm). Interestingly, the pristine sample showed mean and standard deviation of pore diameter values lower than the PTL-pore-area region, resulting from higher volume fractions of smaller pore sizes. Finally, log normal distribution functions were fit to the PSDs and the log normal mean and standard deviation were reported as parameters that can be used for future modeling studies.

Declaration of competing interest

The authors declare that they have no known competing financial interests or personal relationships that could have appeared to influence the work reported in this paper.

Acknowledgments

This work was authored in part by the National Renewable Energy Laboratory, operated by Alliance for Sustainable Energy, LLC, for the U.S. Department of Energy (DOE) under Contract No. DE-AC36-08GO28308. Funding provided by the U.S. Department of Energy Office of Energy Efficiency and Renewable Energy (EERE) Hydrogen and Fuel Cell Technologies Office (HFTO). The views expressed in the article do not necessarily represent the views of the DOE or the U.S. Government. The U.S. Government retains and the publisher, by accepting the article for publication, acknowledges that the U.S. Government retains a nonexclusive, paid-up, irrevocable, worldwide license to publish or reproduce the published form of this work, or allow others to do so, for U.S. Government purposes.

The nano-CT instrument was acquired with the support of a Major Research Instrumentation award from the National Science Foundation under Grant No. 1229090. The pFIB-SEM instrument was acquired with the support of a Major Research Instrumentation award from the National Science Foundation under Grant No. 1428480. The authors acknowledge use of the Materials Characterization Facility at Carnegie Mellon University supported by grant MCF-677785. The authors also thank Dr. Leiming Hu for providing valuable resources for image-processing.

Appendix A. Supplementary data

Supplementary material related to this article can be found online at https://doi.org/10.1016/j.ijhydene.2024.02.020.

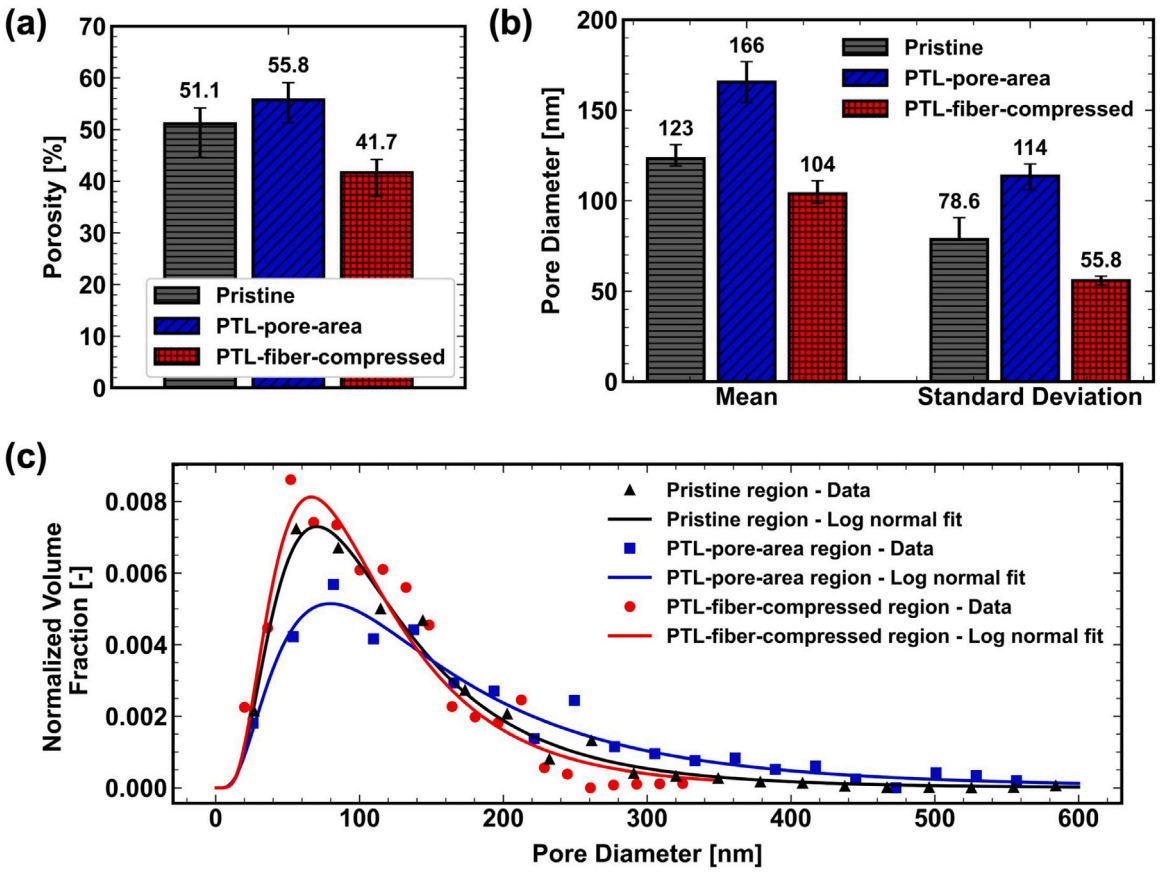

Fig. 8. (a) Comparison of porosities between the three regions of interest. (b) Comparison of mean and standard deviation of pore diameters extracted from the PSDs. The upper and lower bounds of the error bars represent the root mean square error of the upper and lower bounds from the sensitivity analysis. (c) PSDs for the three regions of interest. Each data set was fit to a log normal distribution using Eq. (1). The log normal fit parameters are reported in Table 1.

References

[1] Pivovar B, Rustagi N, Satyapal S. Hydrogen at scale (H 2 @Scale): Key to a clean, economic, and sustainable energy system. J Electrochem Soc 2018;27:47–52. http://dx.doi.org/10.1149/2.F04181if.

[2] Ayers K, Danilovic N, Ouimet R, Carmo M, Pivovar B, Bornstein M. Perspectives on low-temperature electrolysis and potential for renewable hydrogen at scale. Annu Rev Chem Biomol Eng 2019;10:219–39. http://dx.doi.org/10.1146/annurev-chembioeng-060718-030241.

[3] Carmo M, Fritz DL, Mergel J, Stolten D. A comprehensive review on PEM water electrolysis. Int J Hydrogen Energy 2013;38:4901–34. http://dx.doi.org/10.1016/j.ijhydene.2013.01.151.

[4] Ayers K. High efficiency PEM water electrolysis: enabled by advanced catalysts, membranes, and processes. Curr Opin Chem Eng 2021;33:100719. http://dx.doi.org/10.1016/J.COCHE.2021.100719.

[5] Wang Y, Diaz DFR, Chen KS, Wang Z, Adroher XC. Materials, technological status, and fundamentals of PEM fuel cells – a review. Mater Today 2020;32:178–203. http://dx.doi.org/10.1016/j.mattod.2019.06.005.

[6] Danilovic N, Subbaraman R, Chang KC, Chang SH, Kang YJ, Snyder J, Paulikas AP, Strmcnik D, Kim YT, Myers D, Stamenkovic VR, Markovic NM. Activity-stability trends for the oxygen evolution reaction on monometallic oxides in acidic environments. J Phys Chem Lett 2014;5:2474–8. http://dx.doi.org/10.1021/jz501061n.

[7] Minke C, Suermann M, Bensmann B, Hanke-Rauschenbach R. Is iridium demand a potential bottleneck in the realization of large-scale PEM water electrolysis? Int J Hydrogen Energy 2021;46:23581–90. http://dx.doi.org/10.1016/j.ijhydene.2021.04.174.

[8] Taie Z, Peng X, Kulkarni D, Zenyuk IV, Weber AZ, Hagen C, Danilovic N. Pathway to complete energy sector decarbonization with available iridium resources using ultralow loaded water electrolyzers. ACS Appl Mater Interfaces 2020;12:52701–12. http://dx.doi.org/10.1021/acsami.0c15687.

[9] Maier M, Smith K, Dodwell J, Hinds G, Shearing PR, Brett DJ. Mass transport in PEM water electrolysers: A review. Int J Hydrogen Energy 2022;47:30–56. http://dx.doi.org/10.1016/j.ijhydene.2021.10.013.

[10] Mauger SA, Wang M, Cetinbas FC, Dzara MJ, Park J, Myers DJ, Ahluwalia RK, Pylypenko S, Hu L, Litster S, Neyerlin KC, Ulsh M. Development of high-performance roll-to-roll-coated gas-diffusion-electrode-based fuel cells. J Power Sources 2021;506:230039. http://dx.doi.org/10.1016/J.JPOWSOUR.2021.230039.

[11] Wang M, Medina S, Ochoa-Lozano J, Mauger S, Pylypenko S, Ulsh M, Bender G. Visualization, understanding, and mitigation of process-induced-membrane irregularities in gas diffusion electrode-based polymer electrolyte membrane fuel cells. Int J Hydrogen Energy 2021;46:14699–712. http://dx.doi.org/10.1016/j.ijhydene.2021.01.186.

[12] Medina S, Foster JG, Dzara MJ, Wang M, Ulsh M, Mauger SA, Pylypenko S. Multi-technique characterization of spray coated and roll-to-roll coated gas diffusion fuel cell electrodes. J Power Sources 2023;560:232670. http://dx.doi.org/10.1016/j.jpowsour.2023.232670.

[13] Wargo EA, Kotaka T, Tabuchi Y, Kumbur EC. Comparison of focused ion beam versus nano-scale X-ray computed tomography for resolving 3-D microstructures of porous fuel cell materials. J Power Sources 2013;241:608–18. http://dx.doi.org/10.1016/j.jpowsour.2013.04.153.

[14] Shojaeefard MH, Molaeimanesh GR, Nazemian M, Moqaddari MR. A review on microstructure reconstruction of PEM fuel cells porous electrodes for pore scale simulation. Int J Hydrogen Energy 2016;41:20276–93. http://dx.doi.org/10.1016/j.ijhydene.2016.08.179.

[15] Epting WK, Gelb J, Litster S. Resolving the three-dimensional microstructure of polymer electrolyte fuel cell electrodes using nanometer-scale X-ray computed tomography. Adv Funct Mater 2012;22:555–60. http://dx.doi.org/10.1002/adfm.201101525.

[16] Mahbub R, Hsu T, Epting WK, Nuhfer NT, Hackett GA, Abernathy H, Rollett AD, Graef MD, Litster S, Salvador PA. A method for quantitative 3D mesoscale analysis of solid oxide fuel cell microstructures using xe-plasma focused ion beam (PFIB) coupled with SEM. ECS Trans 2017;78:2159–70. http://dx.doi.org/10.1149/07801.2159ECST/XML.

[17] Hsu T, Epting WK, Mahbub R, Nuhfer NT, Bhattacharya S, Lei Y, Miller HM, Ohodnicki PR, Gerdes KR, Abernathy HW, Hackett GA, Rollett AD, Graef MD, Litster S, Salvador PA. Mesoscale characterization of local property distributions in heterogeneous electrodes. J Power Sources 2018;386:1–9. http://dx.doi.org/10.1016/j.jpowsour.2018.03.025.

[18] Joos J, Carraro T, Weber A, Ivers-Tiffée E. Reconstruction of porous electrodes by FIB/SEM for detailed microstructure modeling. J Power Sources 2011;196:7302–7. http://dx.doi.org/10.1016/j.jpowsour.2010.10.006.

[19] Alia SM, Reeves KS, Baxter JS, Cullen DA. The impact of ink and spray variables on catalyst layer properties, electrolyzer performance, and electrolyzer durability. J Electrochem Soc 2020;167:144512. http://dx.doi.org/10.1149/1945-7111/ABC746.

[20] Khandavalli S, Park JH, Kariuki NN, Zaccarine SF, Pylypenko S, Myers DJ, Ulsh M, Mauger SA. Investigation of the microstructure and rheology of iridium oxide catalyst inks for low-temperature polymer electrolyte membrane water electrolyzers. ACS Appl Mater Interfaces 2019;11:45068–79. http://dx.doi.org/10.1021/ACSAMI.9B14415.

[21] Rozain C, Mayousse E, Guillet N, Millet P. Influence of iridium oxide loadings on the performance of PEM water electrolysis cells: Part II - Advanced oxygen electrodes. Appl Catal B 2016;182:123–31. http://dx.doi.org/10.1016/j.apcatb.2015.09.011.

[22] Regmi YN, Tzanetopoulos E, Zeng G, Peng X, Kushner DI, Kistler TA, King LA, Danilovic N. Supported oxygen evolution catalysts by design: Toward lower precious metal loading and improved conductivity in proton exchange membrane water electrolyzers. ACS Catal 2020;10:13125–35. http://dx.doi.org/10.1021/ACSCATAL.0C03098.

[23] Böhm D, Beetz M, Gebauer C, Bernt M, Schröter J, Kornherr M, Zoller F, Bein T, Fattakhova-Rohlfing D. Highly conductive titania supported iridium oxide nanoparticles with low overall iridium density as OER catalyst for large-scale PEM electrolysis. Appl Mater Today 2021;24:101134. http://dx.doi.org/10.1016/J.APMT.2021.101134.

[24] Lewinski KA, van der Vliet D, Luopa SM. NSTF advances for PEM electrolysis - the effect of alloying on activity of NSTF electrolyzer catalysts and performance of NSTF based PEM electrolyzers. ECS Trans 2015;69:893–917. http://dx.doi.org/10.1149/06917.0893ecst.

[25] Hegge F, Lombeck F, Ortiz EC, Bohn L, Holst MV, Kroschel M, Hu J, Breitwieser M, Strasser P, Vierrath S. Efficient and stable low iridium loaded anodes for PEM water electrolysis made possible by nanofiber interlayers. ACS Appl Energy Mater 2020;2020:8276–84. http://dx.doi.org/10.1021/acsaem.0c00735.

[26] Kim Y-T, Lopes PP, Park S-A, Lee A-Y, Lim J, Lee H, Back S, Jung Y, Danilovic N, Stamenkovic V, Erlebacher J, Snyder J, Markovic NM. Balancing activity, stability and conductivity of nanoporous core-shell iridium/iridium oxide oxygen evolution catalysts. Nature Commun 2017;8:1–8. http://dx.doi.org/10.1038/s41467-017-01734-7.

[27] Kulkarni D, Huynh A, Satjaritanun P, O'Brien M, Shimpalee S, Parkinson D, Shevchenko P, DeCarlo F, Danilovic N, Ayers KE, Capuano C, Zenyuk IV. Elucidating effects of catalyst loadings and porous transport layer morphologies on operation of proton exchange membrane water electrolyzers. Appl Catal B 2022;308. http://dx.doi.org/10.1016/j.apcatb.2022.121213.

[28] Majasan JO, Iacoviello F, Cho JI, Maier M, Lu X, Neville TP, Dedigama I, Shearing PR, Brett DJ. Correlative study of microstructure and performance for porous transport layers in polymer electrolyte membrane water electrolysers by X-ray computed tomography and electrochemical characterization. Int J Hydrogen Energy 2019;44:19519–32. http://dx.doi.org/10.1016/j.ijhydene.2019.05.222.

[29] Peng X, Satjaritanun P, Taie Z, Wiles L, Keane A, Capuano C, Zenyuk IV, Danilovic N. Insights into interfacial and bulk transport phenomena affecting proton exchange membrane water electrolyzer performance at ultra-low iridium loadings. Adv Sci 2021;2102950. http://dx.doi.org/10.1002/ADVS.202102950.

[30] Satjaritanun P, O'Brien M, Kulkarni D, Shimpalee S, Capuano C, Ayers KE, Danilovic N, Parkinson DY, Zenyuk IV. Observation of preferential pathways for oxygen removal through porous transport layers of polymer electrolyte water electrolyzers. iScience 2020;23. http://dx.doi.org/10.1016/j.isci.2020.101783.

[31] Leonard E, Shum AD, Danilovic N, Capuano C, Ayers KE, Pant LM, Weber AZ, Xiao X, Parkinson DY, Zenyuk IV. Interfacial analysis of a PEM electrolyzer using X-ray computed tomography. Sustain Energy Fuels 2020;4:921–32. http://dx.doi.org/10.1039/c9se00364a.

[32] Tkachuk A, Duewer F, Cui H, Feser M, Wang S, Yun W. X-ray computed tomography in Zernike phase contrast mode at 8 keV with 50-nm resolution using Cu rotating anode X-ray source. Z Kristallogr 2007;222:650–5. http://dx.doi.org/10.1524/zkri.2007.222.11.650.

[33] Braaten JP, Ogawa S, Yarlagadda V, Kongkanand A, Litster S. Studying Pt-based fuel cell electrode degradation with nanoscale X-ray computed tomography. J Power Sources 2020;478:229049. http://dx.doi.org/10.1016/j.jpowsour.2020.229049.

[34] Litster S, Epting WK, Wargo EA, Kalidindi SR, Kumbur EC. Morphological analyses of polymer electrolyte fuel cell electrodes with nano-scale computed tomography imaging. Fuel Cells 2013;13:935–45. http://dx.doi.org/10.1002/FUCE.201300008.

[35] Mandal P, Epting W, Litster S. Nano- scale X-ray computed tomography: Morphological analysis of fuel cell electrodes. Microsc Microanal 2013;19:630–1. http://dx.doi.org/10.1017/S143192761300514X.

[36] Komini Babu S, Mohamed AI, Whitacre JF, Litster S. Multiple imaging mode X-ray computed tomography for distinguishing active and inactive phases in lithium-ion battery cathodes. J Power Sources 2015;283:314–9. http://dx.doi.org/10.1016/j.jpowsour.2015.02.086.

[37] Komini Babu S, Chung HT, Zelenay P, Litster S. Resolving electrode morphology's impact on platinum group metal-free cathode performance using nano-CT of 3D hierarchical pore and ionomer distribution. ACS Appl Mater Interfaces 2016;8:32764–77. http://dx.doi.org/10.1021/acsami.6b08844.

[38] Kumar AS, Mandal P, Zhang Y, Litster S. Image segmentation of nanoscale Zernike phase contrast X-ray computed tomography images. J Appl Phys 2015;117:183102. http://dx.doi.org/10.1063/1.4919835.

[39] Uddin A, Dunsmore L, Zhang H, Hu L, Wu G, Litster S. High power density platinum group metal-free cathodes for polymer electrolyte fuel cells. ACS Appl Mater Interfaces 2020;12:2216–24. http://dx.doi.org/10.1021/acsami.9b13945.

[40] Hegge F, Moroni R, Trinke P, Bensmann B, Hanke-Rauschenbach R, Thiele S, Vierrath S. Three-dimensional microstructure analysis of a polymer electrolyte membrane water electrolyzer anode. J Power Sources 2018;393:62–6. http://dx.doi.org/10.1016/j.jpowsour.2018.04.089.

[41] Lopata J, Kang Z, Young J, Bender G, Weidner JW, Shimpalee S. Effects of the transport/catalyst layer interface and catalyst loading on mass and charge transport phenomena in polymer electrolyte membrane water electrolysis devices. J Electrochem Soc 2020;167:064507. http://dx.doi.org/10.1149/1945-7111/ab7f87.

[42] Gostick J, Khan Z, Tranter T, Kok M, Agnaou M, Sadeghi M, Jervis R. PoreSpy: A python toolkit for quantitative analysis of porous media images. J Open Source Softw 2019;4:1296. http://dx.doi.org/10.21105/joss.01296.

[43] Schuler T, Schmidt TJ, Büchi FN. Polymer electrolyte water electrolysis: Correlating performance and porous transport layer structure: Part II. Electrochemical performance analysis. J Electrochem Soc 2019;166:F555–65. http://dx.doi.org/10.1149/2.1241908jes.

[44] Xie Z, Yu S, Yang G, Li K, Ding L, Wang W, Zhang FY. Optimization of catalyst-coated membranes for enhancing performance in proton exchange membrane electrolyzer cells. Int J Hydrogen Energy 2021;46:1155–62. http://dx.doi.org/10.1016/J.IJHYDENE.2020.09.239.

[45] Park J, Kang Z, Bender G, Ulsh M, Mauger SA. Roll-to-roll production of catalyst coated membranes for low-temperature electrolyzers. J Power Sources 2020;479:228819. http://dx.doi.org/10.1016/j.jpowsour.2020.228819.

[46] Zydney AL, Aimarb P, Meirelesb M, Pimbley JM, Belfortd G. Use of the log-normal probability density function to analyze membrane pore size distributions: functional forms and discrepancies. J Membr Sci 1994;9:293–8. http://dx.doi.org/10.1016/0376-7388(94)80090-1.

[47] Weber AZ, Darling RM, Newman J. Modeling two-phase behavior in PEFCs. J Electrochem Soc 2004;151:A1715. http://dx.doi.org/10.1149/1.1792891.

[48] Weber AZ. Improved modeling and understanding of diffusion-media wettability on polymer-electrolyte-fuel-cell performance. J Power Sources 2010;195:5292–304. http://dx.doi.org/10.1016/j.jpowsour.2010.03.011.

[49] Hwang GS, Weber AZ. Effective-diffusivity measurement of partially-saturated fuel-cell gas-diffusion layers. J Electrochem Soc 2012;159:F683–92. http://dx.doi.org/10.1149/2.024211jes.

[50] Zenyuk IV, Kumbur EC, Litster S. Deterministic contact mechanics model applied to electrode interfaces in polymer electrolyte fuel cells and interfacial water accumulation. J Power Sources 2013;241:379–87. http://dx.doi.org/10.1016/j.jpowsour.2013.03.165.

[51] Zenyuk IV, Parkinson DY, Connolly LG, Weber AZ. Gas-diffusion-layer structural properties under compression via X-ray tomography. J Power Sources 2016;328:364–76. http://dx.doi.org/10.1016/j.jpowsour.2016.08.020.

[52] Tranter TG, Gostick JT, Burns AD, Gale WF. Pore network modeling of compressed fuel cell components with OpenPNM. Fuel Cells 2016;16:504–15. http://dx.doi.org/10.1002/fuce.201500168.

[53] Zhou J, Shukla S, Putz A, Secanell M. Analysis of the role of the microporous layer in improving polymer electrolyte fuel cell performance. Electrochim Acta 2018;268:366–82. http://dx.doi.org/10.1016/j.electacta.2018.02.100.

[54] Olesen AC, Frensch SH, Kær SK. Towards uniformly distributed heat, mass and charge: A flow field design study for high pressure and high current density operation of PEM electrolysis cells. Electrochim Acta 2019;293:476–95. http://dx.doi.org/10.1016/j.electacta.2018.10.008.

[55] Xu Y, Zhang G, Wu L, Bao Z, Zu B, Jiao K. A 3-D multiphase model of proton exchange membrane electrolyzer based on open-source CFD. Digit Chem Eng 2021;1:100004. http://dx.doi.org/10.1016/j.dche.2021.100004.

[56] Wu W, Jiang F. Microstructure reconstruction and characterization of PEMFC electrodes. Int J Hydrogen Energy 2014;39:15894–906. http://dx.doi.org/10.1016/j.ijhydene.2014.03.074.

[57] Molaeimanesh GR, Bamdezh MA, Nazemian M. Impact of catalyst layer morphology on the performance of PEM fuel cell cathode via lattice Boltzmann simulation. Int J Hydrogen Energy 2018;43:20959–75. http://dx.doi.org/10.1016/j.ijhydene.2018.09.076.

[58] Malekian A, Salari S, Stumper J, Djilali N, Bahrami M. Effect of compression on pore size distribution and porosity of PEM fuel cell catalyst layers. Int J Hydrogen Energy 2019;44:23396–405. http://dx.doi.org/10.1016/j.ijhydene.2019.07.036.

[59] Xie B, Zhang G, Xuan J, Jiao K. Three-dimensional multi-phase model of PEM fuel cell coupled with improved agglomerate sub-model of catalyst layer. Energy Convers Manage 2019;199. http://dx.doi.org/10.1016/j.enconman.2019.112051.

[60] Inoue G, Yokoyama K, Ooyama J, Terao T, Tokunaga T, Kubo N, Kawase M. Theoretical examination of effective oxygen diffusion coefficient and electrical conductivity of polymer electrolyte fuel cell porous components. J Power Sources 2016;327:610–21. http://dx.doi.org/10.1016/j.jpowsour.2016.07.107.

[61] Lee JK, Bazylak A. Optimizing porous transport layer design parameters via stochastic pore network modelling: Reactant transport and interfacial contact considerations. J Electrochem Soc 2020;167:013541. http://dx.doi.org/10.1149/1945-7111/ab6557.